Lawrence Berkeley National Laboratory
LBL Publications

Title
Fluorination effect for stabilizing cationic and anionic redox activities in cation-disordered cathode materials

Permalink
https://escholarship.org/uc/item/41h133bj

Authors
Zhou, Ke
Zheng, Shiyao
Ren, Fucheng
et al.

Publication Date
2020-11-01

DOI
10.1016/j.ensm.2020.07.012

Peer reviewed

eScholarship.org Powered by the California Digital Library
University of California

Fluorination effect for stabilizing cationic and anionic redox activities in cation-disordered cathode materials

Ke Zhou[a], Shiyao Zheng[b], Fucheng Ren[c], Jue Wu[a, d], Haodong Liu[e,*], Mingzeng Luo[a], Xiangsi Liu[a], Yuxuan Xiang[a], Chunyang Zhang[f], Wanli Yang[d], Lunhua He[g], Yong Yang[a,c*]

[a]State Key Laboratory for Physical Chemistry of Solid Surfaces, and Department of Chemistry, College of Chemistry and Chemical Engineering, Xiamen University, Xiamen 361005, China

** Email: yyang@xmu.edu.cn, haodong.liu.xmu@gmail.com*

[b]Department of Mechanical and Nuclear Engineering, The Pennsylvania State University, University Park, PA 16802, USA

[c]School of Energy, Xiamen University, Xiamen 361005, China

[d]Advanced Light Source, Lawrence Berkeley National Laboratory, 1 Cyclotron Road, Berkeley, California 94720, USA

[e]Department of Nanoengineering, University of California San Diego, La Jolla 92093, USA

[f]Laboratory of Photonics and Interfaces, Institute of Chemical Sciences and Engineering, School of Basic Sciences, École Polytechnique Fédérale de Lausanne, Lausanne CH-1015, Switzerland

[g]Dongguan Neutron Science Center, Dongguan 523803, China

Keywords: Cation-disordered Li-excess cathodes, Fluorine-substitution, Anionic redox, Cyclability, Voltage decay

ABSTRACT

Cation-disordered Li-excess cathodes with oxygen redox reactions are promising candidates for high-energy-density Li ion batteries. Nevertheless, the oxygen redox process that is required for the high capacity often comes with the oxygen loss, which leads to severe capacity degradation and voltage decay. In this work, we have successfully synthesized a series of Li-excess cation-disordered cathodes ($Li_{1.2}Mn_{0.4+x}Ti_{0.4-x}O_{2-x}F_x$) ($0 \leq x \leq 0.2$) with different fluorine (F) contents. The electrochemical performance results show that the $Li_{1.2}Mn_{0.55}Ti_{0.25}O_{1.85}F_{0.15}$ (LMTOF0.15) exhibits the highest reversible capacity (275 mAh g^{-1}, under 30 mA g^{-1}), cyclability, and voltage retentions. The mapping of resonant inelastic X-ray scattering (mRIXS) and differential electrochemical mass spectroscopy (DEMS) results reveal that the fluorination enhances the reversible lattice oxygen redox reaction while suppressing irreversible gas release and surface reactions. The X-ray Absorption Spectroscopy (XAS) during the initial two cycles shows that F-substitution alleviates the reduction of the Mn valence state during the whole (dis)charge processes in the bulk and at the surface of the material, results in higher average discharge voltage. In addition, the introduction of F improves the structural stability and suppresses local lattice distortion of the material. Therefore, LMTOF0.15 is able to cycle with smaller polarization, less interfacial side reaction and Mn dissolution, and therefore results in enhanced cyclability. This work provides a comprehensive understanding of the fluorination effect on the cationic and anionic redox activities in cation-disordered Li-excess cathodes.

1. Introduction

The demand of high-energy-density and low-cost cathode materials for high performance Li-ion batteries (LIBs) is increasing, due to the rapid growing of the electrical vehicles market. [1, 2] At present, the classical transition metal (TM) layered oxides (such as $LiCoO_2$, $LiNi_xCo_yMn_{1-x-y}O_2$) and $LiFePO_4$ dominate the cathode markets. [3-5] However, the performance of these materials is limited by the cationic redox reaction, with some of them reach almost the theoretical limits. [6-8] As a comparison, the Li-excess materials ($Li_{1+x}TM_{1-x}O_2$) deliver much higher capacities of > 300 mAh g^{-1}, which is attributed to the participation of the anionic redox processes. [3, 9] Li-excess materials create linear Li-O-Li configurations in which the O 2p orbitals do not hybridize with a TM orbital, and the higher energy of these labile O 2p states makes them easier to trigger the oxidation of O^{2-} to O^{-} or the release of O_2. [10] Recently, Ceder and Yabuuchi et al. unlocked the cation-disordered Li-excess cathode materials for LIBs, which possess abundance redox reactions from both TM (Cr^{3+}/Cr^{5+}, Mn^{3+}/Mn^{4+}, Ni^{2+}/Ni^{4+}, Mn^{2+}/Mn^{4+}, Mo^{3+}/Mo^{6+}, Fe^{3+}/Fe^{4+}, V^{3+}/V^{5+}) and O (e.g., O^{2-}/O_2^{n-}), leading to high capacities. [11-17]

Up to now, cation-disordered Li-excess materials such as $Li_{1.3}Nb_{0.3}Mn_{0.4}O_2$, [15] $Li_{1.2}Ti_{0.4}Mn_{0.4}O_2$, [6, 18] $Li_{1.2}Ni_{1/3}Ti_{1/3}Mo_{2/15}O_2$ [12] and $Li_{1.3}Ta_{0.3}Mn_{0.4}O_2$ [19] have attracted a lot of research attentions, which are capable of delivering reversible capacity of higher than 300 mAh g^{-1}. However, almost all of the reported cation-disordered cathodes suffer from the large voltage hysteresis and fast capacity fade induced by the TM cations migration and severe oxygen loss upon cycling. [20-25] Therefore, tuning oxygen reaction is the key towards better performance. Recently, substitution of part O^{2-} ions by F^{-} ions was proposed as an effective way to enhance cycling stability and reduce the oxygen loss from the cation-disordered compounds. [26-30] For instance, $Li_{1.15}Ni_{0.45}Ti_{0.3}Mo_{0.1}O_{1.85}F_{0.15}$ (LNF15) contains more redox-active TM (Ni^{2+}) and less oxygen redox compared with $Li_{1.15}Ni_{0.375}Ti_{0.375}Mo_{0.1}O_2$ (LN15), which leads to an increase in TM redox reservoir and less oxygen oxidation. [30] They also showed that $Li_2Mn_{1/2}Ti_{1/2}O_2F$ and $Li_2Mn_{2/3}Nb_{1/3}O_2F$ exhibit better cycling stabilities than their F free analogs. It was proposed that combining the reversible Mn^{2+}/Mn^{4+} two-electrons redox couple and the partial F-substitution of O in cation-disordered oxides cathode can produce high capacity. [26] However, the detailed fluorination effect for enhancing the electrochemical performance of these cathode materials remains elusive. In addition, the effects of F-substitution on the cationic and anionic redox processes have not been comprehensively clarified. Therefore, a comparative study of the fluorination on redox mechanism and the structural evolution during cycling is crucial to both understand and to achieve excellent cyclability and voltage retention performances of cation-disordered compounds.

In this work, $Li_{1.2}Mn_{0.4}Ti_{0.4}O_{0.2}$ (LMTO) and a series of F-substituted Li-excess cation-disordered cathodes ($LMTO_{2-x}F_x$) were prepared. The $Li_{1.2}Mn_{0.55}Ti_{0.25}O_{1.85}F_{0.15}$ (LMTOF0.15) exhibits less capacity and voltage decay than LMTO. Multiple characterization techniques (e.g. XRD, DEMS, XAS, mRIXS, etc.) combined with first-principles calculations are used to study their cationic and anionic redox activities, and structure evolution (average & local) upon cycling. We found that F-substitution suppresses irreversible oxygen loss, which significantly mitigate the Mn valence reduction and structural degradation. In addition, a LiF-rich protective layer was also formed to protect the surface of the material.

2. Experimental

2.1 Material synthesis

A solid-state method was used for synthesizing all the cation-disordered Li-excess oxides including $Li_{1.2}Mn_{0.4}Ti_{0.4}O_2$ (LMTO), $Li_{1.2}Mn_{0.45}Ti_{0.35}O_{1.95}F_{0.05}$ (LMTOF0.05), $Li_{1.2}Mn_{0.5}Ti_{0.3}O_{1.9}F_{0.1}$ (LMTOF0.1), $Li_{1.2}Mn_{0.55}Ti_{0.25}O_{1.85}F_{0.15}$ (LMTOF0.15) and $Li_{1.2}Mn_{0.6}Ti_{0.2}O_{1.8}F_{0.2}$ (LMTOF0.2). Stoichiometric amounts of Li_2CO_3 (10 wt % excess, Sinopharm Chemical Reagent Co., Ltd. ≥98.0%), Mn_2O_3 and TiO_2 (Alfa Aesar, 99.0%) and LiF (Aladdin Industrial Corporation, 99.9%) were firstly grinded and then ball milled at 300 rpm for 6h via a planetary ball milling machine (QM-3SP04, Nanjing Nanda Instrument Plant). The mixture was then dried and pressed into pellets and was calcined at 950 °C for 16 h in an inert Ar atmosphere followed by natural cooling down in the furnace. The pellet was then ground into fine powder and mixed with acetylene black (AB) (samples: AB = 90:10 wt%) by using a planetary ball mill for 24 hours at a speed of 500 rpm in a zirconia container.

2.2 Electrochemical measurements

All electrochemical tests were conducted in CR2025 coin-type cells. The active material, acetylene black (AB) and poly(-vinylidene fluoride) binder (PVDF) were ball milled in a weight ratio of 8:1:1 in N-methyl-2-pyrrolidene (NMP) solvent to obtain the slurry, which was then cast on an aluminum foil and used as the positive electrode. 1 M $LiPF_6$/EC-EMC (3:7 by vol.) (Shenzhen CAPCHEM Co., Ltd. (China)) was used as the electrolyte. The cells were assembled in an argon-filled glovebox, using Li metal as the negative electrode. Galvanostatic tests were performed on a LAND (CT-2001A, Wuhan, China) battery test system.

2.3 Material characterization

The powder and *ex-situ* X-ray diffraction (XRD) patterns were recorded with a Rigaku Ultima IV powder X-ray diffractometer using Cu Kα radiation (λ = 1.5406 Å). The Neutron powder diffraction (NPD) data were collected at the beamline of general purpose powder diffractometer (GPPD) at the China Spallation Neutron Source (CSNS). Rietveld refinement against the neutron diffraction was performed using General Structure Analysis System (GSAS) software with EXPGUI interface to obtain the lattice and atomic parameters of the powder samples. [31] Morphological features of the samples were observed using a scanning electron microscope (SEM, ZEISS Sigma, Germany) with an energy-dispersive X-ray spectroscopy (EDS) detector used for EDS elemental mapping, operating at 15 kV, and conducted on a scanning transmission electron microscope (TEM, F-20, FEI, Netherlands), operating at 200 kV. The exact compositions of Mn and Ti were determined by using Optima 2000-DV inductively coupled plasma emission spectrometry (ICP-OES, Perkin Elmer, United States).

A custom-built differential electrochemical mass spectrometer measurement (DEMS, Hiden, United Kingdom) and the cell geometry used are described in previous publications. [6, 32] The cell assembly was conducted in an Ar glovebox. High purity Ar at a speed of 0.5 mL min^{-1} was used as the carrier gas upon cycling.

The mapping of resonant inelastic X-ray scattering (mRIXS) experiments were performed in the high-efficiency iRIXS endstation at Beamline 8.0.1 of Advanced Light

Source (ALS) at Lawrence Berkeley National Laboratory. [33] All the RIXS data were collected under ultrahigh vacuum through the high-resolution spectrometer with an excitation energy steps of 0.2 eV. [34] The resolution of the excitation energy and emission energy are about 0.35 eV and 0.25 eV, respectively. Both entrance and exit slits of beamline monochromater were set as 40/40 to control the energy resolution of incident X-ray beam. The recorded spectra were measured from the side of electrode facing the current collector and then plotted in color scale. The TiO_2 was used as reference sample of a series O K-edge spectra. Final two-dimensional mRIXS images were obtained via background subtraction, energy calibration, normalization and a multistep data processing in a previous study. [35]

The *ex-situ* hard X-ray absorption spectrum (hXAS) data were collected in transmission mode at a room temperature, using ion chamber detectors at beamline BL14W1 of the Shanghai Synchrotron Radiation Facility (SSRF) and a Si (111) double-crystal monochromator. The focal spot size at the position of the sample was 0.25 mm. The monochromators were calibrated to reject higher harmonics of the selected wavelength (harmonic content < 10^{-4}) and data were collected over a range of energies, from 200 eV below to 500 eV above the Mn (6539 eV) and Ti (4979 eV) K-edges, respectively. The incident photon energy was calibrated with Mn/Ti metal foils just prior to data collection in all measurements. The soft X-ray absorption spectrum (sXAS) were collected in electron yield modes at beamline 4B7B (O/F K-edge and Mn/Ti L-edge) of the Beijing Synchrotron Radiation Facility (BEPC). The postedge background was determined using a cubic spline procedure. Processing and fitting of the all XAS data were performed using an Athena software. [36]

2.4 First Principles Calculations

First-principle calculations were performed with a plane basic set and the projector augmented method, as implemented in the Vienna Ab Initio Simulation Package. [37, 38] The exchange-correlation interactions were treated with the generalized gradient approximation (GGA) and PBE function. [39] The effects generated by the localization of d electrons of TM ions were also taken into account by the GGA +U approach of Dudarev et al. [40] The cutoff energy was set to be 550 eV. Brillouin-zone integrations are approximated by using special k-point sampling of Monkhorst-Pack scheme [41] with the k-point mesh of 3×3×1. The convergence criterion for the electronic self-consistency loop was set to 10^{-5} eV, and atomic positions were relaxed until atomic forces were less than 0.05 eV Å^{-1}.

3. Results and Discussion

3.1. Crystal Structure, Morphology, and Electronic Structure Characterizations

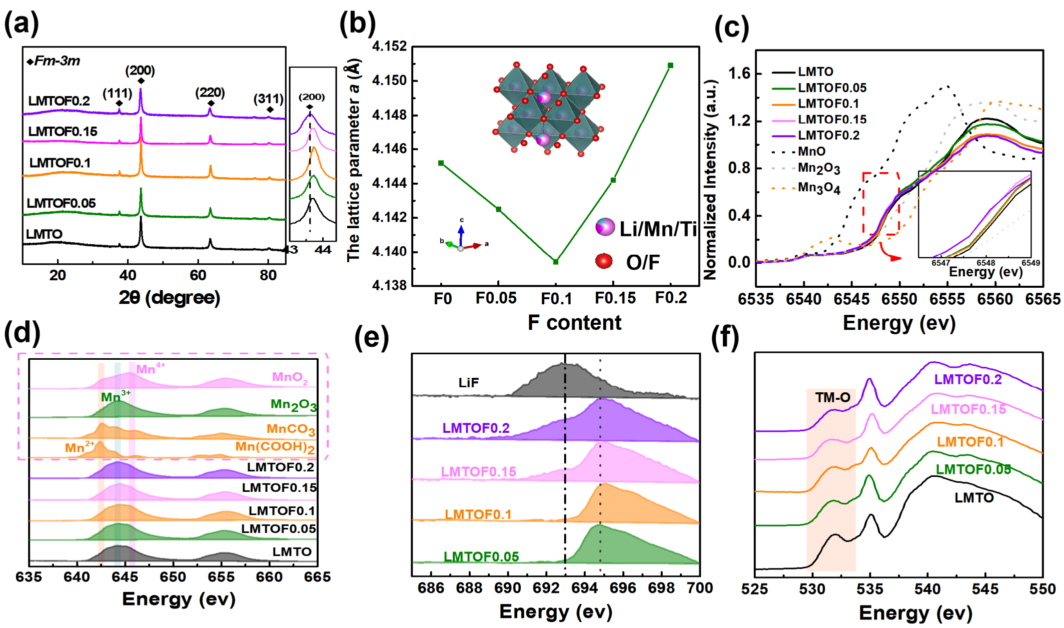

Fig. 1. (a) XRD patterns (λ = 1.5406 Å) of LMTO, LMTOF0.05, LMTOF0.1, LMTOF0.15 and LMTOF0.2. (b) The refined lattice parameter *a* of all materials. Insert figure is a schematic diagram of cation-disordered $LMTO_{2-x}F_x$ cathode materials. XAS spectra of all materials. (c) Mn K-edge. (d) Mn L-edge. (e) F K-edge. (f) O K-edge.

Fig. 1a shows the powder XRD patterns of $LMTO_{2-x}F_x$ (x=0, 0.05, 0.1, 0.15, 0.2). All samples can be indexed as the cation-disordered rock-salt phase (*Fm-3m*). The magnification of the (200) reflection highlights the effect of F-substitution on the lattice parameters. The lattice parameter *a* of LMTO is 4.1452(2) Å (**Fig. 1**b), while for LMTOF0.05 and LMTOF0.1 the lattice parameter *a* slightly decreases (4.1425(3) Å and 4.1394(8) Å, respectively), which is due to the smaller ionic radius of F^{-} (r = 1.33 Å) compared with that of O^{2-} (r = 1.40 Å). [30] Meanwhile, the replacement of Ti^{4+} (r = 0.605 Å) by Mn^{3+} (r = 0.58 Å) also reduces the lattice parameters. As for LMTOF0.15 and LMTOF0.2, the lattice parameter *a* is slightly larger than that of LMTOF0.1, which is attributed to the presence of small amounts of Mn^{2+} (r = 0.67 Å). The ICP results in **Table SI 1** confirm the chemical composition of the synthesized materials and show that the Mn/Ti ratio is slightly less than the designed value for high F content materials. Therefore, it can be considered that the existence of Mn^{2+} is account for balancing the charge of the material. The SEM images of all samples are shown in **Figs. SI 1**a-e, which consist of irregular polyhedral particles with an average particle size of approximately 1 μm. F uniformly distributes throughout the LMTOF0.15 particle is clarified by energy dispersive spectroscopy (EDS) (**Figs. SI 1**f-h).

The electronic structures of TM/F/O in the bulk and at the surface are detected by hXAS and sXAS. [18, 42] All L/K-edge of TM/F/O absorption spectra of $LMTO_{2-x}F_x$ powder samples were displayed in **Figs. 1**c-f **and Fig. SI 2.** The Mn K-edge energy (**Fig. 1**c) of LMTO, LMTOF0.05, LMTOF0.1 and LMTOF0.15 are all close to Mn_2O_3 (Mn^{3+} reference), and shifts to lower energy for LMTOF0.15 and LMTOF0.2. This indicates that the oxidation state of Mn in the bulk slightly decreases with the increase of F content, which is consistent with the XRD and ICP results. The TEY model used in the sXAS test has a good response to the material surface (detecting depth is nearly 10 nm). [42-44] According to the sXAS results, the oxidation states of surface Mn and Ti remain +3 and +4 for all materials(**Fig. 1**d **and Fig. SI 2**). The F K-edge spectra in **Fig. 1**e shows the existence of LiF at the surface of LMTOF0.15 and LMTOF0.2. The TEM images(**Fig. SI3**) reveals that the surface of the LMTOF0.15 is covered by a thin layer of LiF. The pre-edge features (orange region) in O K-edge sXAS (**Fig. 1**f**)** represent the TM-O hybridization states. The decreasing pre-edge peak intensity from LMTO to LMTOF0.2 indicates a reduced TM-O hybridization as the F content increases. In summary, the F is successfully introduced into the bulk of LMTOF0.05 and LMTOF0.1, while partial of the F forms LiF on the surface of the LMTOF0.15 and LMTOF0.2.

3.2. Electrochemical test

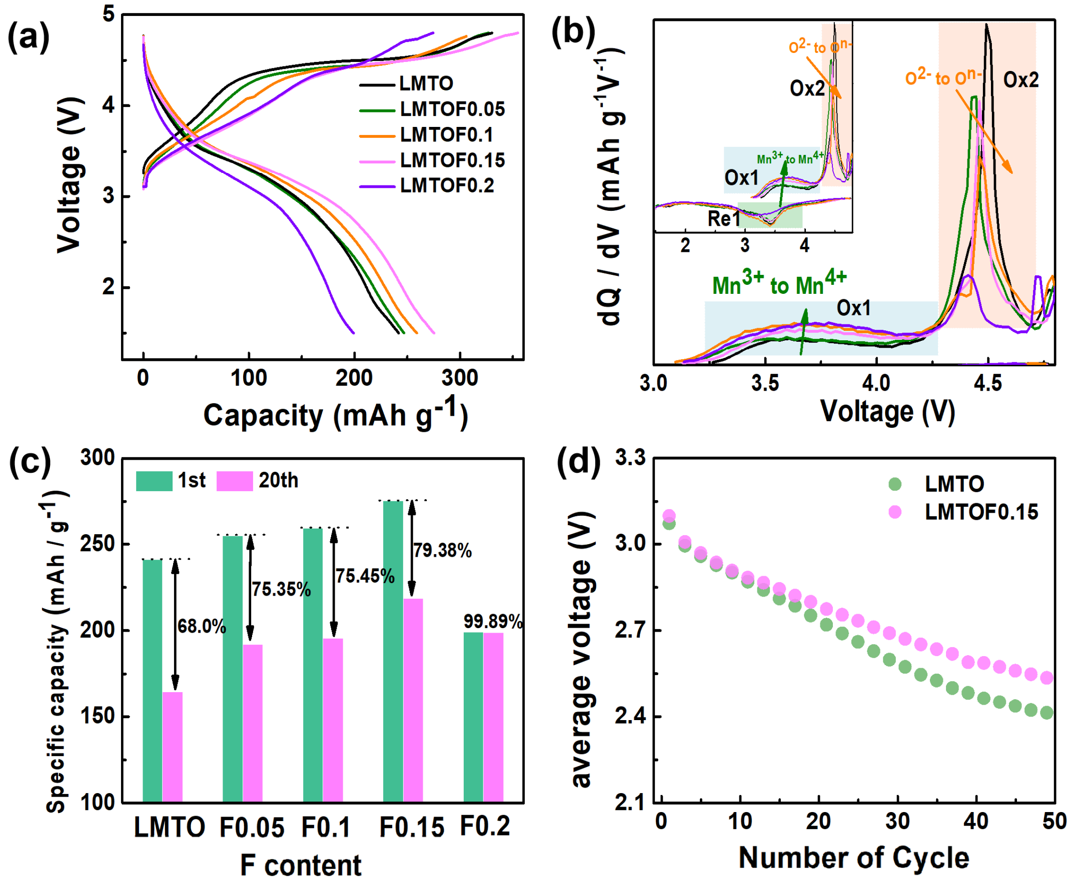

Fig. 2. (a) The first cycle voltage profiles of the LMTO, LMTOF0.05, LMTOF0.1, LMTOF0.15 and LMTOF0.2 between 1.5 and 4.8 V under current density of 30 mA g^{-1} at room temperature. (b) Corresponding dQ/dV curves for Figure 2(a). (c) Comparison of discharge capacities of all materials at the 1^{st} and 20^{th} cycle between 1.5 and 4.8 V under current density of 30 mA g^{-1} at room temperature. The numbers next to the bars represent the capacity retention. (d) Average discharge voltage over the course of 50 cycles of LMTO and LMTOF0.15.

The electrochemical properties of $LMTO_{2-x}F_x$ are compared by galvanostatic cycling them between 1.5 and 4.8 V in **Fig. 2**a. The specific discharge capacities of $LMTO_{2-x}F_x$ (x=0, 0.05, 0.1, 0.15) increases from 241 mAh g^{-1} to 275 mAh g^{-1} as the F content increases to 0.15. Further increasing the F content shows lower initial discharge capacity, for example the LMTOF0.2 delivers low initial discharge capacity of 199 mAh g^{-1}. In order to understand the effect of F on the electrochemical behavior of cationic and anionic redox, the dQ/dV curves of all $LMTO_{2-x}F_x$ materials are shown in **Fig. 2**b. A broad peak centered at around 3.5 V (Mn^{3+}/Mn^{4+}, the slope, Ox1) and a sharp peak at around 4.5 V ($O^{2-}/(O_2)^{n-}$, the long plateau, Ox2) were observed during the first charge process, which corresponds to the two-step redox process reported in previous works. [6] It is notable that Mn oxidation reaction slightly increases (Ox1), while the O oxidation reaction gradually reduces as a function of the F content in the $LMTO_{2-x}F_x$ (Ox2). During the discharge, only a single broad peak (Re1) was observed, which suggests that the reduction of the Mn and O species are coupled. The oxidation of oxygen has been effectively suppressed in LMTOF0.2. The detailed voltage profile and cycling performance of the $LMTO_{2-x}F_x$ are presented in **Figs. SI 4**a-e. After 20 cycles (**Fig. 2**c), LMTO electrode shows a discharge capacity of only 164 mAh g^{-1}, with a low capacity retention of 68%. As a comparison, LMTOF0.05, LMTOF0.1, LMTOF0.15 deliver higher discharge capacities up to 192, 199 and 218 mAh g^{-1}, with capacity retention of 75.35, 75.45 and 79.38%, respectively. The cyclability result in **Fig. SI 5** shows that capacity fading can be mitigated with the F-substitution. Since the LMTOF0.15 delivers the highest specific capacity and capacity retention, it is further characterized to study the mechanism of F-substitution. **Fig. 2**d shows the average voltages of LMTO and LMTOF0.15. The average voltage equals energy density divided by capacity. Clearly, the voltage fading of LMTOF0.15 (ΔE=0.48 V) is inhibited compared with that of LMTO (ΔE=0.60 V) for the first 50 cycles. All the electrochemical tests show that F-substitution improves the (dis)charge specific capacity, capacity retention and alleviates voltage decay.

3.3. The anionic redox activity

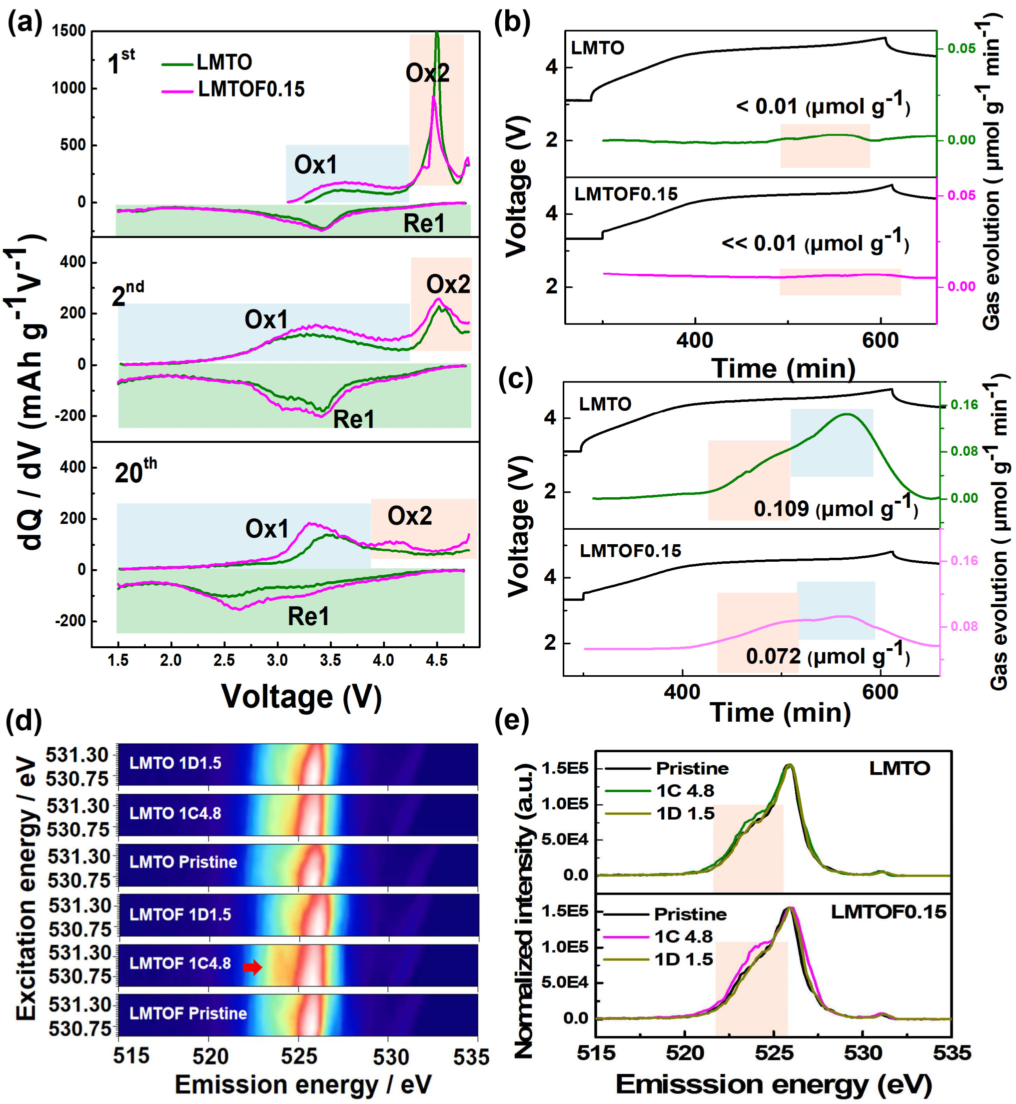

Fig. 3. (a) The dQ/dV curves at the 1st, 2nd and 20th cycles of LMTO and LMTOF0.15 between 1.5 and 4.8V under current density of 30 mA g^{-1}. Operando DEMS results of O_2 (b) and CO_2 (c) for LMTO and LMTOF0.15, respectively. (d) The O K-edge mRIXS images of LMTO and LMTOF0.15 electrodes at representative electrochemical states. The red arrows indicate the oxygen oxidation state that is clearer in LMTOF0.15 than LMTO. (e) The RIXS spectra of LMTO and LMTOF0.15 collected with 531 eV excitation energy. The intensity in the orange shaded area corresponds to the oxidized oxygen triggered

by oxygen redox reaction at the charged state. “1C/D” represents first charged/discharged state.

The dQ/dV curves of the LMTO and the LMTOF0.15 are compared to better understand their cationic and anionic redox behavior. For the first charge process, the capacity provided by TM oxidation (Ox1 region) for LMTOF0.15 is higher than that of LMTO, while the capacity from oxygen oxidation (Ox2 region) is less (**Fig. 3**a**)**. At the second cycle, the Ox2 peak of LMTOF0.15 is stronger than LMTO, indicating that oxygen redox provides more reversible capacity in LMTOF0.15. In particular, the Ox2 peak in LMTO almost diminishes after 20 cycles, while the LMTOF clearly shows the anionic oxidation activity. This result implies that F-substitution improves the reversibility of oxygen redox process, which contributes to the better cyclability. The voltage profiles of two materials with various cutoff voltages of 4.3 and 4.8 V are presented in **Figs. SI 6**a,b. There is almost no capacity loss below 4.3V with only the Mn redox process. Once the O activity involves into the whole electrochemical process, serious capacity decay is observed (4.8 V). Therefore, it is concluded that the capacity decay is mainly induced by the oxygen oxidation. The LMTOF0.15 electrode material shows less capacity decay within the voltage range of 1.5V to 4.8V.

Operando DEMS and *ex-situ* mRIXS measurements are conducted on LMTO and LMTOF0.15 to directly monitor both the irreversible (released) and the reversible (redox in lattice) oxygen activities, respectively. [45, 46] **Figs 3**b, c present the DEMS results of the two materials. At the end of the first charge, the amount of O_2 generated from LMTOF0.15 is less than that of LMTO (orange region), indicating more irreversible oxygen loss in the form of O_2 for LMTO. Besides, a noticeable amount of CO_2 gas generation (0.109 and

0.072 μmol mg^{-1}) were detected on both LMTO and LMTOF0.15. According to the literature, at least 70% of CO_2 gas evolution is attributed to surface carbonate decomposition (e.g. Li_2CO_3) between 3.8 and 4.0 V (orange region). [26] The remaining CO_2 gas generated at a high voltage presumably originates from the electrolyte oxidized by surface oxygen (blue region). [30, 45] The DEMS results show that LMTOF0.15 material produced less O_2 and CO_2, indicating the LMTOF0.15 features less irreversible oxygen loss and less surface side reactions than those of the LMTO.

The mRIXS has been developed as a powerful tool to detect the lattice oxygen reaction by resolving the energy distribution of the emitted photons at the sXAS absorption edges. [46] In general, the O mRIXS results are dominated by broad and strong vertical features centered around 525 eV emission energy from the hybridization between O 2p and TM-*d* states. Meanwhile, a mRIXS feature at around 531 eV excitation energy and 523.7 eV emission energy is a fingerprint of the oxidized oxygen, [46] which has been found in model non-divalent oxygen systems such as Li_2O_2 and O_2. [46, 47] **Fig. 3**e displays the key mRIXS fingerprinting portion of the oxidized oxygen feature around 531 eV excitation energy, with the full maps of the representative samples shown in **Fig. SI 7**. The comparison between the LMTO and LMTOF0.15 at the fully charged states (1C 4.8V) shows directly that the oxidized oxygen feature of LMTOF0.15 is much stronger than that in LMTO, as indicated by the red arrow on **Fig. 3**d. This contrast could be better seen in the RIXS spectra collected at 531 eV excitation energy, which are over-plotted together in **Fig. 3**e, where the oxidized oxygen feature of LMTOF0.15 in the shaded area is much more prominent when the electrode is at the charged state. It is important to note that, the oxidized oxygen signals of mRIXS are from the lattice oxygen that is fundamentally different from the irreversible O_2 release and surface reactions. [48] Indeed, contrasting the relatively less gas evolution in the DEMS results of LMTOF0.15 compared with LMTO, the lattice oxidized oxygen is much stronger in LMTOF0.15, and displays a reversible oxygen redox reaction, indicated by the disappearance of the clear oxidized oxygen feature when the electrode is discharged (1D 1.5V). Therefore, the F in LMTOF0.15 suppresses the irreversible gas evolution and electrolyte decomposition, while enhances the reversible oxygen redox reactions in the system.

3.4. The cationic redox activity

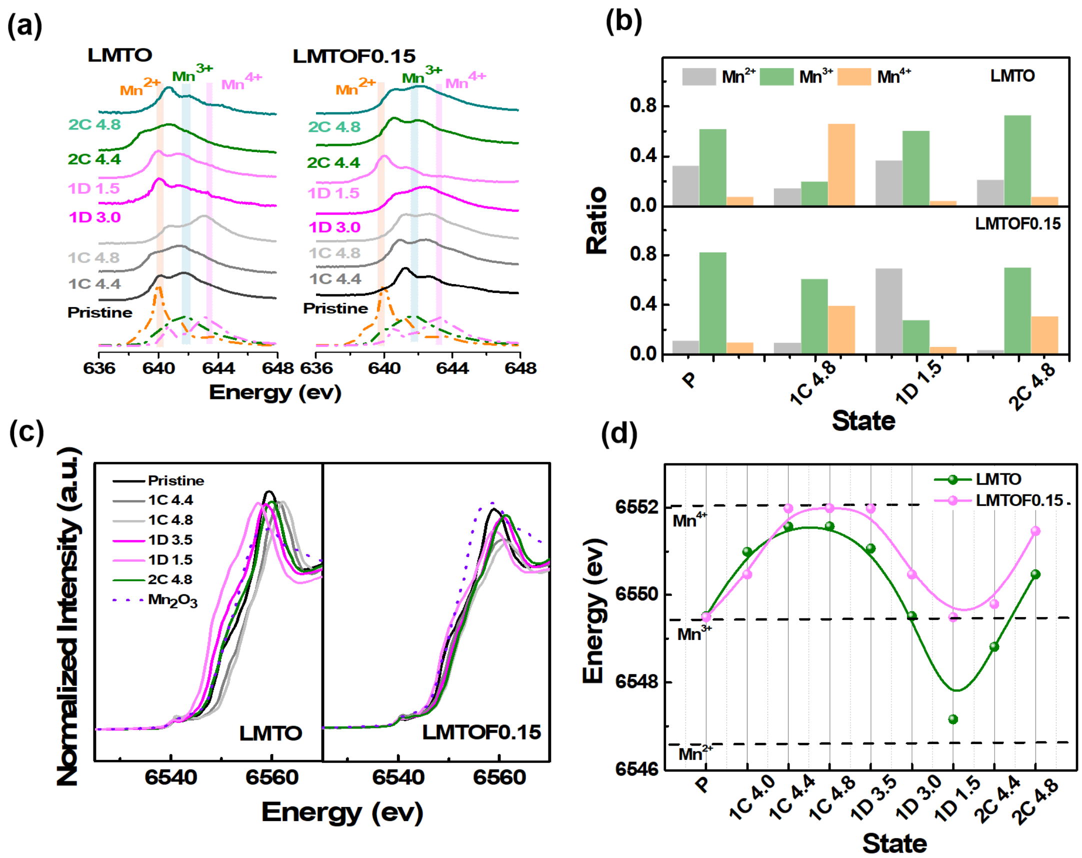

Fig. 4. (a) Oxidation state evolution of Mn at the surface of LMTO and LMTOF0.15 in the 1st and 2nd cycles charge at 30 mA g^{-1} by sXAS. The pristine electrodes have been immersed in the electrolyte for 8

hours. 1C and 1D represent first charging and discharging processes, respectively. (b) The quantitative analysis of Mn oxidation states change based on the fitted Mn L-edge sXAS spectra in Fig. S8b. The error is below ± 3 percentage estimated from the uncertainty in the fitting procedure. (c) Oxidation state evolution of Mn in the bulk for LMTO and LMTOF0.15 in the 1st cycle and 2nd charge at 30 mA g^{-1} by hXAS. (d) Average Mn oxidation state (determined from XANES absorption energies) as a function of different states of charge.

sXAS and X-ray absorption near-edge structure (XANES) measurements are employed to investigate the cationic redox activity at the surface and in the bulk during the initial and second charge cycles. [18, 42, 49] **Fig. 4**a gives the oxidation state evolution of Mn at the surface of LMTO and LMTOF0.15, and the quantitative analysis [22] based on the fitted Mn L-edge sXAS spectra (**Fig. SI 8**) is in **Fig. 4**b. About 32% Mn^{2+}, 61% Mn^{3+} and 7% Mn^{4+} are found at the surface of pristine LMTO electrode, which was soaked into the electrolyte for 8 hours. The presence of Mn^{2+} and Mn^{4+} can be ascribed to the reactive interface. The trace amount of HF and other acidic species formed by the oxidation of carbonate solvents lead to the disproportion of Mn^{3+}, and then Mn dissolves after charging process. [50, 51] The fully charged (1C 4.8V) LMTO electrode exhibits about 68% Mn^{4+}, 19% Mn^{3+} and 13% Mn^{2+}. The formation of Mn^{3+} and Mn^{2+} is possibly caused by partial reduction of Mn^{4+} or some chemical reaction between Mn^{4+} and exited $O^{(2-x)-}$ species. In addition, the electrolyte is prone to be oxidized and decomposed at high voltage, accompanying with severe side reactions with TM. [12, 52] During the discharge process, more Mn^{3+} and Mn^{2+} are generated. The fully discharged (1D 1.5V) electrode shows about 36% Mn^{2+}, 60% Mn^{3+} and 4% Mn^{4+}, respectively. At the fully charged state in 2nd cycle (2C

4.8V), there is only about 7% Mn^{4+}. This may be due to the violent surface reaction forming a thick and dense layer (oxygen deficient structure) , reducing the valence state of Mn. [53, 54] For LMTOF0.15 material, the LiF protective layer prevents the material from acid attacking, so that Mn^{3+} disproportion is alleviated. As a result, the Mn of the LMTOF0.15 pristine material contains Mn^{2+} (10%), Mn^{3+} (81%) and Mn^{4+} (9%), and Mn^{4+} (38%) at 1C 4.8V. The fully discharged (1D 1.5V) electrode have about Mn^{2+} (68%), Mn^{3+} (26%) and Mn^{4+} (6%). At the second fully charged state (2C 4.8V) shows about 29% Mn^{4+}, obviously more than the Mn^{4+} at the surface of the LMTO. At the same time, the TM in these compounds dissolves into the electrolyte and diffuses to the lithium metal anode and separator as evidenced by the presence of Mn/Ti ion shown in the ICP-OES measurements (**Table SI 2)**. The dissolved substances have been considered as MnO or manganese ion compound and will further transform to other stable manganese oxides. [55] We also deduce that irreversible lattice oxygen loss at the surface would lead to surface reconstruction in LMTO, which will destabilize the Mn-O bond and eventually cause Mn dissolution. Significantly lower concentration of dissolved cations (Mn) are detected in the case of LMTOF0.15 compared with LMTO upon cycling. Therefore, the less oxygen loss and the LiF protection layer of LMTOF0.15 material suppress the TM dissolution (**Table SI 2)** and improve the capacity retention. The Ti dissolution also occurs. The little change of shape and position for LMTO Ti L-edges at 1D 1.5V indicates that Ti actually reacts with the electrolyte (**Fig. SI 9**). The LMTOF0.15 (**Fig. SI 9**b) result suggests that the Ti^{4+} is stable during (dis)charge processes.

Fig. 4c shows the Mn K-edge XANES of LMTO and LMTOF0.15 at various voltages. For both materials, bulk Mn^{3+} is oxidized towards Mn^{4+} during charge, and a reverse reduction process occurs upon discharge. However, Mn oxidation state in LMTOF0.15 are higher than LMTO during the entire (dis)charge processes according to **Fig. 4**d, especially at fully charged (1C 4.8 V) and discharged (1D 1.5V) states. There are two reasons for the higher Mn valence state of LMTOF0.15. The less irreversible loss of lattice oxygen of LMTOF0.15 maintains more Mn^{4+} at the fully charged state. The other reason is that the content of Mn in LMTO is 27% less than that in LMTOF. It seems that the Mn in LMTO is further reduced to compensate the charge during the lithiation process, which will lead to the reduction of Mn^{3+} to Mn^{2+} during the discharge. Therefore, the Mn valence in LMTOF0.15 is close to Mn^{3+} at the fully discharged state, while the Mn in LMTO is below +3. For the electrodes at the second cycles, Mn valence state in the bulk of LMTOF0.15 is higher than that of LMTO, indicating that F-substitution alleviates the reduction of the Mn valence to the Mn^{2+}. Therefore, the Re1 region of dQ/dV curves in **Fig. 3**a presents that the discharge voltage of LMTOF0.15 is higher than that of LMTO, which is also reflected in the discharge voltage profiles (**Fig. 2**d).

From the perspective of the cationic redox activity for LMTO and LMTOF0.15, it clearly shows that F-substitution alleviates the reduction of the Mn^{4+} to the Mn^{3+}/Mn^{2+} during charge process and Mn^{3+} to Mn^{2+} during discharge process. Therefore, LMTOF0.15 exhibits an optimal cyclability and voltage retention.

3.5. Structural evolution upon cycling

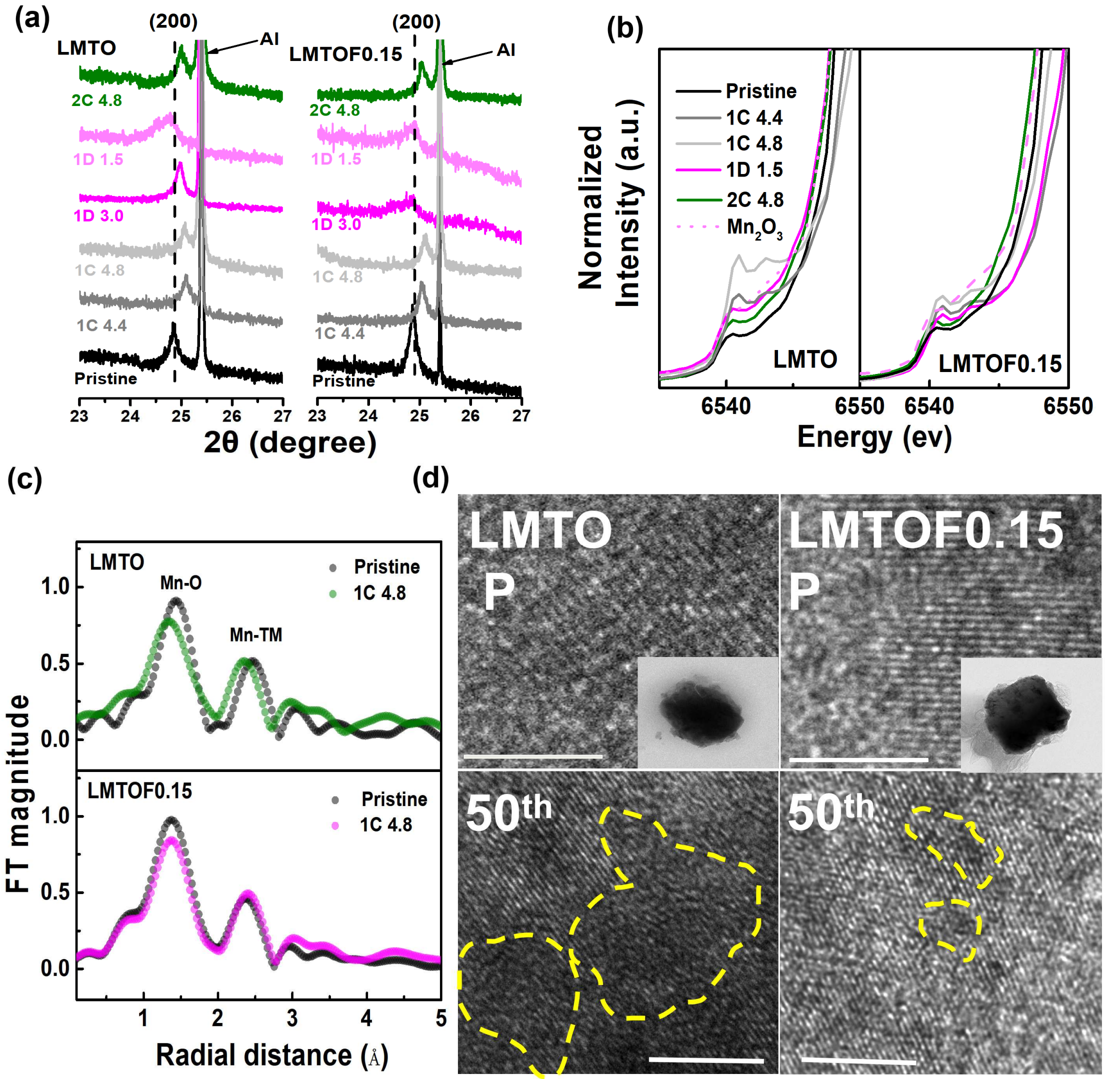

Fig. 5. (a) *Ex-situ* XRD patterns of LMTO and LMTOF0.15 during the 1st and 2nd cycles. (b) Mn K-edge pre-edge hXAS spectra of LMTO and LMTOF0.15. (c) The Fourier-transformed k^3-weighted EXAFS spectra. The first peak corresponds to the first shell of Mn-O coordination. (d) The high resolution TEM image for pristine and after 50 cycles of LMTO and LMTOF0.15. The scale bar is 5 nm.

To investigate the structural evolution of LMTO and LMTOF0.15, *ex-situ* XRD of the two materials were carried out. As displayed in **Fig. 5**a, the (200) diffraction peak of LMTO starts to shift to higher angle at 1C 4.4 V as a result of Mn oxidation (Mn^{3+} to Mn^{4+}). From 4.4 V to 4.8 V there is no obvious peak shift, indicating the lattice parameter a is almost unchanged. During discharge process, the peak shifts to a lower angle. The similar trend can be also observed in LMTOF0.15. Compared to LMTO, a smaller shift of (200) peak is observed on LMTOF0.15, indicating that the lattice parameters of LMTOF0.15 show a relatively smaller variation after one cycle. The pre-edge peak in **Fig. 5**b represents the transition of Mn 1s electron to Mn 3d orbital that is electric dipole forbidden, and thus could not appear in a high-symmetry coordination. [12, 56] From OCV to 1C 4.3 V, the pre-edge peak intensity gradually becomes stronger, suggesting the existence of local lattice structural distortion. From 1C 4.3 V to 1C 4.8 V, distortion of LMTO is significantly enhanced during the oxygen oxidation process. It is probably because the formation of O^{n-} ($n < 2$) or O_2 leads to the structural distortion. [57] During the rest of (dis)charge processes, the pre-edge peak intensity of LMTO is still stronger than that of LMTOF0.15. This result shows the poor structural stability and more severe distortion of LMTO, which affects the cycling performance. Besides, the Fourier-transformed k^3-weighted EXAFS (**Fig. 5**c) displays a great change of Mn-O bond length for LMTO. The Mn-O coordination peak intensity decreases at 1C 4.8 V, which indicates the local structural disorder of the electrode material. [58] The peak intensity of LMTO remains lower than LMTOF0.15, suggesting the local structural disorder is more severe in the LMTO material. In addition, there is a significant change in bond length during the charging of the LMTO electrode. The change in the bond length of LMTOF0.15 is smaller than that of LMTO, indicating that the local structure of LMTOF0.15 is more stable. The TEM images and *ex* situ X-ray diffraction patterns were collected for the pristine and after 50 cycles, as shown in **Figs. 5**d and **S10**. The distortion of crystal planes (yellow regions) and the decrease and shift of diffraction peaks of LMTO are more severe than that of LMTOF0.15. These results confirm that the labile activated oxygen in LMTO is easily overoxidized to generate gas results in such large structural variation, indicating that F-substitution effectively stabilizes the structure upon cycling.

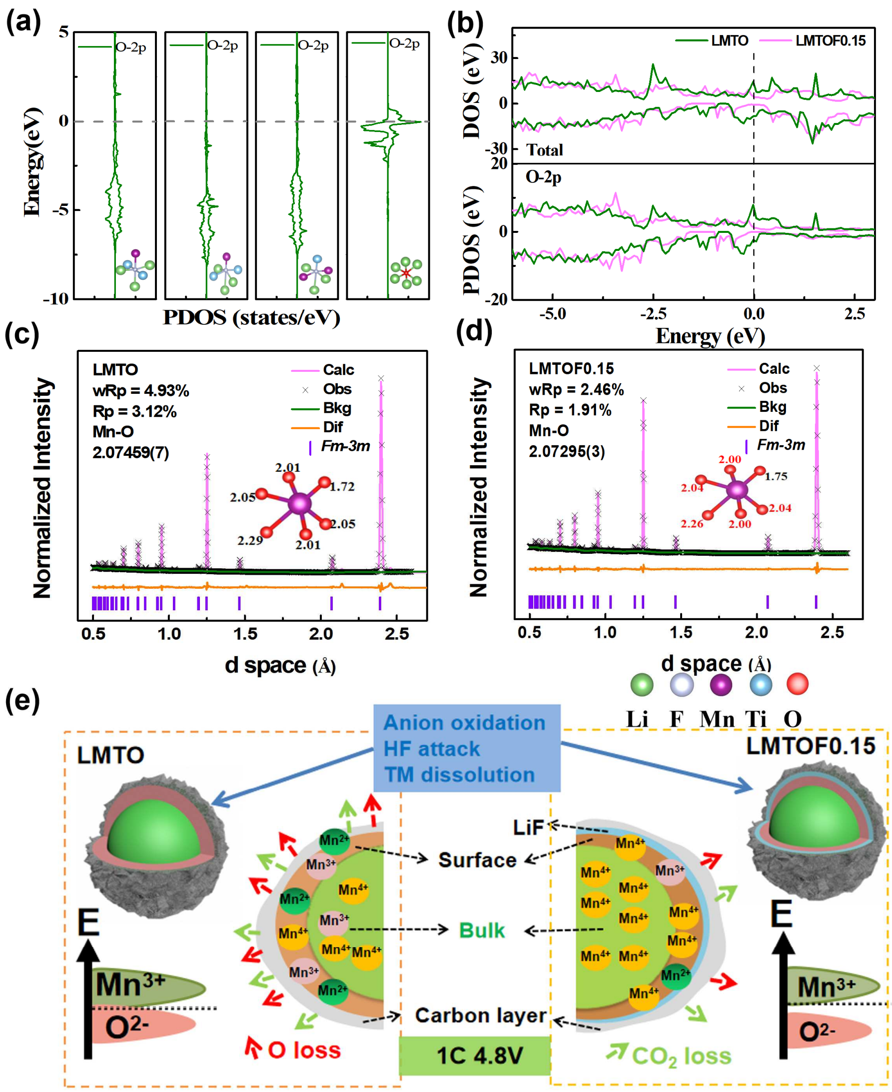

Fig. 6. (a) PDOS of the O 2p orbitals in different O local environments. (b) Total DOS and PDOS of the O 2p orbitals for LMTO and LMTOF0.15. Rietveld refinement of NPD patterns of LMTO (c) and LMTOF0.15 (d). The inset schematic illustration is the result from DFT calculation. (e) Schematic illustration of the structural change and Mn/O ions gradient distribution for LMTO and LMTOF0.15 cathode (first charge 4.8 V).

The electrochemical results show that the LMTOF0.15 delivers higher capacity, coulomb efficiency and capacity retention than the LMTO, which is benefited from the enhanced reversibility of the O redox reaction. There are two main reasons for the increased reversibility of the oxygen reaction. Due to the overlap between TM d orbitals and O 2p orbitals, the increase of Mn redox reaction leads to the decrease of O activity as a result of the competition between TM and O redox reactions. [15, 18] The DFT calculations were carried out to understand the fundamental reasons of oxygen oxidation potential change in LMTO ($Li_{12}Mn_4Ti_4O_{20}$) and LMTOF0.15 ($Li_{12}Mn_5Ti_3O_{19}F_1$). Based on the structural parameters from the diffraction data, a series of LMTO structural units were constructed. Here Li, Mn and Ti atoms are randomly distributed at 4a sites and O is only located at 4b sites. The calculated results of different structure models are displayed in **Figs. SI 11**a, b. The formation energy of #1 structure (**Fig. SI 11**c) with alternating distribution of Mn and Ti is the most stable one compared to other structures. The #1 structure have four different local oxygen environments coordinated by six atoms. To explain the oxygen oxidation, the projected density of states (pDOS) of oxygen 2p states of different oxygen configurations (**Fig. 6**a) are compared. The pDOS of the oxygen 2p states with six Li around is much closer to the Fermi level than that with other configurations. The contribution of pDOS near the Fermi level is largely affected by the M-O orbital interactions. The substitution of O^{2-} by F^{-} is regarded as one O atom substituted by one F. By calculating the formation energies of different F environments (**Fig. S11**d), the lowest formation energies are obtained when F is surrounded by 6 Li from thermodynamic energy. This weaker interaction leads to the decreasing oxygen pDOS below the Fermi level and reducing the above orbitals' overlap, which suggests a less oxygen oxidation (**Fig. 6**b).

From the structural point of view, both the Neutron powder diffraction (NPD) [59] data and DFT results show that the average bond length of TM-O decreases after F-substitution (**Figs. 6**c, d **and Table SI 3**). The shrinkage of TM-O bond distance can increase the covalency of the TM-O bonding and the energy level of hybridized TM d states with antibonding characteristic (e_g*). Due to strong TM-O covalency bond is favorable for the thermodynamic stabilization of the O^- oxidized species, [21, 60] F-substitution material stabilized the structure to prevent overoxidized of O^{2-} to generate O_2. In addition, with the increase of F content, the number of Mn-O bonds gradually decreases as well as the activity of O^{2-}, [61] leading to less oxidation of oxygen anions. Hence, the LMTOF0.15 does lose less oxygen and maintains more reversible oxygen. However, the (dis)charge capacity of LMTOF0.2 is significantly reduced due to the highly mitigated oxygen redox reaction and thick LiF surface layer. Different degree of irreversible oxygen redox reaction and oxygen loss affect the oxidation states of Mn in the bulk and at the surface of electrode material (**Fig. 6**e). The reduction of irreversible oxygen loss after F-substitution increases the amount of Mn^{4+} in the bulk at fully charge state and reduce the formation of Mn^{2+} at fully discharge state. Consequently, the lattice F substitution retains both anionic and cationic redox activities. Finally the surface LiF coating layer also protects the material from reacting with the electrolyte and dissolving the TM from the surface.

4. Conclusion

This comprehensive study reveals the fluorination effect on the electrochemical performance improvement of cation-disordered cathode materials. The electrochemical tests, DEMS and mRIXS showed the F-substitution enhances the reversible lattice oxygen redox reaction while suppressing the irreversible oxygen release and surface reactions. Thus improves cyclability, and voltage retention. In addition, the LMTOF exhibits higher oxidation state of Mn than the LMTO during (dis)charge process, which is another reason that alleviates the voltage decay. XRD, TEM, and EXAFS spectra results indicate that this F-substitution strategy also mitigates structural distortion during (dis)charge process. NPD data and DFT results prove that F-substitution can stabilize TM-O bonds of material to reduce oxygen release. The formation of surface LiF layer is another protection for the electrode from etching by acidic species in the electrolyte or other parasitic reactions and suppressing the TM dissolution. With all the positive effects of the F-substitution, LMTOF0.15 material exhibits much better cyclability and voltage retention. In summary, F-substitution, as one effective strategy, could mitigate the oxygen loss of the electrode, suppress the side surface reactions, and stabilize the surface/interface structure upon cycling.

Acknowledgements

This work is financially supported by National Key Research and Development Program of China (grant no. 2018YFB0905400), National Natural Science Foundation of China (Grant No. 21935009, 21761132030) and Collaboration project between Ningde City & Xiamen University (2017c002). The authors sincerely thank the assistance of the

Beijing/Shanghai Synchrotron Radiation Facility and the National Synchrotron Radiation Laboratory for the beamtime and help for the hard X-ray absorption spectroscopy. The resonant inelastic X-ray scattering experiments were performed at the Advanced Light Source at Lawrence Berkeley National Laboratory, a US DOE Office of Science User Facility, WY's effort on DRX materials is supported by DOE EERE VTO under the Applied Battery Materials Program, both under contract No. DE-AC02-05CH11231. The authors are very indebted to Dr. Lunhua He, China Spallation Neutron Source (CSNS), Dongguan, China, for their help on the neutron powder diffraction experiments at GPPD.

References

[1] J.B. Goodenough, Y. Kim, Challenges for Rechargeable Li Batteries, Chem. Mater. 22 (2010) 587-603.

[2] J. M. Tarascon, M. Armand, Issues and challenges facing rechargeable lithium batteries, Nature 414 (2001) 358-367.

[3] S. Hy, H. Liu, M. Zhang, D. Qian, B.-J. Hwang, Y.S. Meng, Performance and design considerations for lithium excess layered oxide positive electrode materials for lithium ion batteries, Energy Environ. Sci. 9 (2016) 1931-1954.

[4] P.K. Nayak, E.M. Erickson, F. Schipper, T.R. Penki, N. Munichandraiah, P. Adelhelm, H. Sclar, F. Amalraj, B. Markovsky, D. Aurbach, Review on challenges and recent advances in the electrochemical performance of high capacity Li- and Mn-rich cathode materials for Li-Ion batteries, Adv. Energy Mater. 8 (2018) 1702397.

[5] A. Manthiram, A reflection on lithium-ion battery cathode chemistry, Nat. Commun 11 (2020).

[6] K. Zhou, S. Zheng, H. Liu, C. Zhang, H. Gao, M. Luo, N. Xu, Y. Xiang, X. Liu, G. Zhong, Y. Yang, Elucidating and mitigating the degradation of cationic-anionic redox processes in $Li_{1.2}Mn_{0.4}Ti_{0.4}O_2$ cation-disordered cathode materials, ACS appl. Mater. Interfaces 11 (2019) 45674-45682.

[7] W. Lee, S. Muhammad, C. Sergey, H. Lee, J. Yoon, Y.-M. Kang, W.-S. Yoon, Advances in the cathode materials for making a breakthrough in the Li rechargeable batteries Angew. Chem. Int. Ed. 59 (2019) 2578-2605.

[8] Q. Liu, X. Su, D. Lei, Y. Qin, J. Wen, F. Guo, Y.A. Wu, Y. Rong, R. Kou, X. Xiao, F. Aguesse, J. Bareño, Y. Ren, W. Lu, Y. Li, Approaching the capacity limit of lithium cobalt oxide in lithium ion batteries via lanthanum and aluminium doping, Nat. Energy (2018).

[9] S. Zheng, F. Zheng, H. Liu, G. Zhong, J. Wu, M. Feng, Q. Wu, W. Zuo, C. Hong, Y. Chen, K. An, P. Liu, S. Wu, Y. Yang, Novel ordered rocksalt-type lithium-rich $Li_2Ru_{1-x}Ni_xO_{3-\delta}$ ($0.3 \le x \le 0.5$) cathode material with tunable anionic redox potential, ACS Appl. Energy Mater. 2 (2019) 5933-5944.

[10] D.H. Seo, J. Lee, A. Urban, R. Malik, S. Kang, G. Ceder, The structural and chemical origin of the oxygen redox activity in layered and cation-disordered Li-excess cathode materials, Nat. Chem. 8 (2016) 692-697.

[11] J. Lee, A. Urban, X. Li, D. Su, G. Hautier, G. Ceder, Unlocking the potential of cation-disordered oxides for rechargeable lithium batteries, Science 343 (2014).

[12] J. Lee, D.-H. Seo, M. Balasubramanian, N. Twu, X. Li, G. Ceder, A new class of high capacity

cation-disordered oxides for rechargeable lithium batteries: Li–Ni–Ti–Mo oxides, Energy Environ. Sci. 8 (2015) 3255-3265.
[13] R. Wang, X. Li, L. Liu, J. Lee, D.-H. Seo, S.-H. Bo, A. Urban, G. Ceder, A disordered rock-salt Li-excess cathode material with high capacity and substantial oxygen redox activity: $Li_{1.25}Nb_{0.25}Mn_{0.5}O_2$, Electrochem. Commun. 60 (2015) 70-73.
[14] R.J. Clément, Z. Lun, G. Ceder, Cation-disordered rocksalt transition metal oxides and oxyfluorides for high energy lithium-ion cathodes, Energy Environ. Sci. 13 (2020) 345-373.
[15] N. Yabuuchi, M. Takeuchi, M. Nakayama, H. Shiiba, M. Ogawa, K. Nakayama, T. Ohta, D. Endo, T. Ozaki, T. Inamasu, K. Sato, S. Komaba, High-capacity electrode materials for rechargeable lithium batteries: Li_3NbO_4-based system with cation-disordered rocksalt structure, Proc. Natl. Acad. Sci. U.S.A. 112 (2015) 7650-7655.
[16] N. Yabuuchi, M. Takeuchi, S. Komaba, S. Ichikawa, T. Ozaki, T. Inamasu, Synthesis and electrochemical properties of $Li_{1.3}Nb_{0.3}V_{0.4}O_2$ as a positive electrode material for rechargeable lithium batteries, Chem. Commun. 52 (2016) 2051-2054.
[17] M. Nakajima, N. Yabuuchi, Lithium-excess cation-disordered rocksalt-type oxide with nanoscale phase segregation: $Li_{1.25}Nb_{0.25}V_{0.5}O_2$, Chem. Mater. 29 (2017) 6927-6935.
[18] N. Yabuuchi, M. Nakayama, M. Takeuchi, S. Komaba, Y. Hashimoto, T. Mukai, H. Shiiba, K. Sato, Y. Kobayashi, A. Nakao, M. Yonemura, K. Yamanaka, K. Mitsuhara, T. Ohta, Origin of stabilization and destabilization in solid-state redox reaction of oxide ions for lithium-ion batteries, Nat. Commun. 7 (2016) 13814-13822.
[19] W.H. Kan, C. Wei, D. Chen, T. Bo, B.-T. Wang, Y. Zhang, Y. Tian, J.-S. Lee, Y. Liu, G. Chen, Evolution of Local Structural Ordering and Chemical Distribution upon Delithiation of a Rock Salt-Structured $Li_{1.3}Ta_{0.3}Mn_{0.4}O_2$ Cathode, Adv. Funct. Mater. 29 (2019) 1808294.
[20] D. Chen, W.H. Kan, G. Chen, Understanding performance degradation in cation‐disordered rock‐salt oxide cathodes, Adv. Energy Mater. 9 (2019) 1901255-1901269.
[21] E. Zhao, L. He, B. Wang, X. Li, J. Zhang, Y. Wu, J. Chen, S. Zhang, T. Liang, Y. Chen, X. Yu, H. Li, L. Chen, X. Huang, H. Chen, F. Wang, Structural and mechanistic revelations on high capacity cation-disordered Li-rich oxides for rechargeable Li-ion batteries, Energy Storage Mater. 16 (2019) 354–363.
[22] E. Zhao, Q. Li, F. Meng, J. Liu, J. Wang, L. He, Z. Jiang, Q. Zhang, X. Yu, L. Gu, W. Yang, H. Li, F. Wang, X. Huang, Stabilizing oxygen lattice and reversible oxygen redox chemistry through structural dimensionality in Li-rich cathode oxides, Angew. Chem. Int. Ed. 58 (2019) 4323-4327.
[23] M.A. Cambaz, B.P. Vinayan, H. Geßwein, A. Schiele, A. Sarapulova, T. Diemant, A. Mazilkin, T. Brezesinski, R.J. Behm, H. Ehrenberg, M. Fichtner, Oxygen activity in Li-rich disordered rock-salt oxide and the influence of $LiNbO_3$ surface modification on the electrochemical performance, Chem. Mater. 31 (2019) 4330-4340.
[24] W.H. Kan, B. Deng, Y. Xu, A.K. Shukla, T. Bo, S. Zhang, J. Liu, P. Pianetta, B.-T. Wang, Y. Liu, G. Chen, Understanding the effect of local short-range ordering on lithium diffusion in $Li_{1.3}Nb_{0.3}Mn_{0.4}O_2$ single-crystal cathode, Chem 4 (2018) 2108-2123.
[25] S. Liu, X. Feng, X. Wang, X. Shen, E. Hu, R. Xiao, R. Yu, H. Yang, N. Song, Z. Wang, X. Yang, L. Chen, Another strategy, detouring potential decay by fast completion of cation mixing, Adv. Energy Mater. 8 (2018) 1703092-1703100.
[26] J. Lee, D.A. Kitchaev, D.H. Kwon, C.W. Lee, J.K. Papp, Y.S. Liu, Z.y. Lun, R.J. Clément, T. Shi, B.D. McCloskey, J.h. Guo, M. Balasubramanian, G. Ceder, J.K. Lee, D. A. Kwon, D. H. Lee, C. W. Papp, J. K.

Liu, Y. S. Lun, Z. Clement, R. J. Shi, T. McCloskey, B. D. Guo, J. Balasubramanian, M. Ceder, G., Reversible Mn^{2+}/Mn^{4+} double redox in lithium-excess cathode materials, Nature 556 (2018) 185-190.

[27] R.J. Clément, D. Kitchaev, J. Lee, G. Ceder, Short-range order and unusual modes of nickel redox in a fluorine-substituted disordered rocksalt oxide lithium-ion cathode, Chem. Mater. 30 (2018) 6945-6956.

[28] Z. Lun, B. Ouyang, D.A. Kitchaev, R.J. Clément, J.K. Papp, M. Balasubramanian, Y. Tian, T. Lei, T. Shi, B.D. McCloskey, J. Lee, G. Ceder, Improved cycling performance of li-excess cation-disordered cathode materials upon fluorine substitution, Adv. Energy Mater. 9 (2018) 1802959.

[29] W.D. Richards, S.T. Dacek, D.A. Kitchaev, G. Ceder, Fluorination of lithium-excess transition metal oxide cathode materials, Adv. Energy Mater. 8 (2018) 1701533.

[30] J. Lee, J.K. Papp, R.J. Clement, S. Sallis, D.H. Kwon, T. Shi, W. Yang, B.D. McCloskey, G. Ceder, Mitigating oxygen loss to improve the cycling performance of high capacity cation-disordered cathode materials, Nat. Commun. 8 (2017) 981.

[31] B.H. Toby, EXPGUI, a graphical user interface for GSAS, J. Appl. Crystallogr. 34 (2001) 210-213.

[32] O. Wolter, J. Heitbaum, Differential electrochemical mass spectroscopy (DEMS) -a new method for the study of electrode processes Ber. Bunsenges. Phys. Chem. 88 (1984) 2-6.

[33] R. Qiao, Q. Li, Z. Zhuo, S. Sallis, O. Fuchs, M. Blum, L. Weinhardt, C. Heske, J. Pepper, M. Jones, A. Brown, A. Spucces, K. Chow, B. Smith, P.A. Glans, Y. Chen, S. Yan, F. Pan, L.F. Piper, J. Denlinger, J. Guo, Z. Hussain, Y.D. Chuang, W. Yang, High-efficiency in situ resonant inelastic x-ray scattering (iRIXS) endstation at the advanced light source, Rev. Sci. Instrum. 88 (2017) 033106.

[34] Y.D. Chuang, Y.C. Shao, A. Cruz, K. Hanzel, A. Brown, A. Frano, R. Qiao, B. Smith, E. Domning, S.W. Huang, L.A. Wray, W.S. Lee, Z.X. Shen, T.P. Devereaux, J.W. Chiou, W.F. Pong, V.V. Yashchuk, E. Gullikson, R. Reininger, W. Yang, J. Guo, R. Duarte, Z. Hussain, Modular soft x-ray spectrometer for applications in energy sciences and quantum materials, Rev. Sci. Instrum. 88 (2017) 013110.

[35] J. Wu, S. Sallis, R. Qiao, Q. Li, Z. Zhuo, K. Dai, Z. Guo, W. Yang, Elemental-sensitive detection of the chemistry in batteries through Soft X-ray absorption spectroscopy and resonant inelastic X-ray scattering, JoVE (2018).

[36] B. Ravel, M. Newville, ATHENA, ARTEMIS, HEPHAESTUS: data analysis for X-ray absorption spectroscopy using IFEFFIT, J. Synchrotron Radiat. 12 (2005) 537-541.

[37] J.F. G. Kresse, Efficient iterative schemes for ab initio total-energy calculations using a plane-wave basis set, Phys. Rev. B 54 (1996) 11169-11186.

[38] J.F. G. Kresse, Efficiency of ab-initio total energy calculations for metals and semiconductors using a plane-wave basis set. Comp. Mater. Sci. 6 (1996) 15-50.

[39] J.P. Perdew, K. Burke, M. Ernzerhof, Generalized gradient approximation made simple, Phys. Rev. Lett. 77 (1996) 3865-3868.

[40] S.L. Dudare, G.A. Botton, S.Y. Savraso, C.J. Humphreys, A.P. Sutton, Electron-energy-loss spectra and the structural stability of nickel oxide: An LSDA+U study, Phys. Rev. B 57 (1998) 1505-1509.

[41] D.J. Chadi, Special points for Brillouin-zone integrations, Phys. Rev. B 16 (1977) 1746-1747.

[42] F. Lin, Y. Liu, X. Yu, L. Cheng, A. Singer, O.G. Shpyrko, H.L. Xin, N. Tamura, C. Tian, T.C. Weng, X.Q. Yang, Y.S. Meng, D. Nordlund, W. Yang, M.M. Doeff, Synchrotron X-ray analytical techniques for studying materials electrochemistry in rechargeable batteries, Chem. Rev. 117 (2017) 13123-13186.

[43] B. Li, N. Jiang, W. Huang, H. Yan, Y. Zuo, D. Xia, Thermodynamic activation of charge transfer in anionic redox process for Li-Ion batteries. Adv. Funct. Mater. 28 (2018) 1704864-1704874.

[44] N. Zhang, X. Long, Z. Wang, P. Yu, F. Han, J. Fu, G. Ren, Y. Wu, S. Zheng, W. Huang, C. Wang, H. Li; X. Liu, Mechanism study on the interfacial stability of a lithium garnet-type oxide electrolyte against

cathode materials. ACS Appl. Energy Mater. 1 (2018) 5968-5976.

[45] K. Luo, M.R. Roberts, R. Hao, N. Guerrini, D.M. Pickup, Y.S. Liu, K. Edstrom, J. Guo, A.V. Chadwick, L.C. Duda, P.G. Bruce, Charge-compensation in 3d-transition-metal-oxide intercalation cathodes through the generation of localized electron holes on oxygen, Nat. Chem. 8 (2016) 684-691.

[46] W. Yang, T.P. Devereaux, Anionic and cationic redox and interfaces in batteries: Advances from soft X-ray absorption spectroscopy to resonant inelastic scattering, J. Power Sources 389 (2018) 188-197.

[47] Z. Zhuo, Y.S. Liu, J. Guo, Y.D. Chuang, F. Pan, W. Yang, Full energy range resonant inelastic X-ray scattering of O_2 and CO_2: direct comparison with oxygen redox state in batteries, J. Phys. Chem. Lett 11 (2020) 2618-2623.

[48] J. P. Wu, Z. Q. Zhuo, X. H. Rong, K. H. Dai, Z. Lebens-Higgins, S. Sallis, F. Pan, L. F. J. Piper, G. Liu, Y.D. Chuang, Z. Hussain, Q. H. Li, R. Zeng, Z. X. Shen, W. L. Yang, Dissociate lattice oxygen redox reactions from capacity and voltage drops of battery electrodes Sci. Adv. 6 (2020).

[49] H. Ji, J. Wu, Z. Cai, J. Liu, D.-H. Kwon, H. Kim, A. Urban, J.K. Papp, E. Foley, Y. Tian, M. Balasubramanian, H. Kim, R.J. Clément, B.D. McCloskey, W. Yang, G. Ceder, Ultrahigh power and energy density in partially ordered lithium-ion cathode materials, Nat. Energy 5 (2020) 213-221.

[50] Y.J.S. Dong H. Jang, and Seung M. Oh, Dissolution of spinel oxides and capacity losses in 4 V Li/$Li_xMn_2O_4$ Cells, J. Electrochem. Soc. 143 (1996) 2204-2211.

[51] S.S. Zhang, Problems and their origins of Ni-rich layered oxide cathode materials, Energy Storage Mater. 24 (2020) 247-254.

[52] M. Luo, S. Zheng, J. Wu, K. Zhou, W. Zuo, M. Feng, H. He, R. Liu, J. Zhu, G. Zhao, S. Chen, W. Yang, Z. Peng, Q. Wu, Y. Yang, Identifying the anionic redox activity in cation-disordered $Li_{1.25}Nb_{0.25}Fe_{0.50}O_2$/C oxide cathodes for Li-ion batteries, J. Mater. Chem. A 8 (2020) 5115-5127.

[53] H. Koga, L. Croguennec, M. Ménétrier, P. Mannessiez, F. Weill, C. Delmas, Different oxygen redox participation for bulk and surface: A possible global explanation for the cycling mechanism of $Li_{1.20}Mn_{0.54}Co_{0.13}Ni_{0.13}O_2$, J. Power Sources 236 (2013) 250-258.

[54] H. Chen, M.S. Islam, Lithium extraction mechanism in Li-rich Li_2MnO_3 involving oxygen hole formation and dimerization, Chem. Mater. 28 (2016) 6656-6663.

[55] J. Zheng, M. Gu, J. Xiao, P. Zuo, C. Wang, J.G. Zhang, Corrosion/fragmentation of layered composite cathode and related capacity/voltage fading during cycling process, Nano Lett. 13 (2013) 3824-3830.

[56] T. Okumura, M. Shikano, H. Kobayashi, Effect of bulk and surface structural changes in Li_5FeO_4 positive electrodes during first charging on subsequent lithium-ion battery performance, J. Mater. Chem. A 2 (2014) 11847-11856.

[57] J. Zhang, F. Cheng, S. Chou, J. Wang, L. Gu, H. Wang, H. Yoshikawa, Y. Lu, J. Chen, Tuning oxygen redox chemistry in Li-rich Mn-based layered oxide cathodes by modulating cation arrangement, Adv. Mater. 31 (2019) 1901808-1901814.

[58] J. Rana, M. Stan, R. Kloepsch, J. Li, G. Schumacher, E. Welter, I. Zizak, J. Banhart, M. Winter, Structural changes in Li_2MnO_3 cathode material for Li-ion batteries, Advanced Energy Materials 4 (2014) 1300998.

[59] H. Liu, H. Liu, I. D. Seymour, N. Chernova, K. M. Wiaderek, N. M. S. Trease, Hy, Y. Chen, K. An, M. Zhang, O. J. Borkiewicz, S. H. Lapidus, B. Qiu, Y. Xia, Z. Liu, P. J. Chupas, K. W. Chapman, M. S. Whittingham, C. P. Grey, Y. S. Meng, Identifying the chemical and structural irreversibility in $LiNi_{0.8}Co_{0.15}Al_{0.05}O_2$ – a model compound for classical layered intercalation. J. Mater. Chem. A 6 (2018) 4189-4198.

[60] Y. Xie, M. Saubanère, M.L. Doublet, Requirements for reversible extra-capacityin Li-rich layered oxides for Li-ion batteries, Energy Environ. Sci. 10 (2017) 266-274.

[61] E. Hu, X. Yu, R. Lin, X. Bi, J. Lu, S. Bak, K.-W. Nam, H.L. Xin, C. Jaye, D.A. Fischer, K. Amine, X.-Q. Yang, Evolution of redox couples in Li- and Mn-rich cathode materials and mitigation of voltage fade by reducing oxygen release, Nat. Energy 3 (2018) 690-698.